

Spatiotemporal patterns of temperature inversions and impacts on surface PM_{2.5} across China

Yonglin Fang¹, Hancheng Hu¹, Xiangdong Zheng², Jianping Guo³, Xingbing Zhao⁴, Fang Ma⁵, Hao Wu¹

¹Chengdu University of Information Technology, China Meteorological Administration Radar Meteorology Key Laboratory, Chengdu¹College of Electronic Engineering & Key Laboratory of CMA Atmospheric Sounding, Chengdu University of Information Technology, Chengdu 610225, China

²Chinese Academy of Meteorological Sciences, Beijing 100081, China

³State Key Laboratory of Severe Weather Meteorological Science and Technology & Specialized Meteorological Support Technology Research Center, Chinese Academy of Meteorological Sciences, Beijing 100081, China

⁴Chengdu Institute of Plateau Meteorology, China Meteorological Administration, Chengdu 610072, China

⁵Yunnan Atmospheric Observation Technology Support Center, Kunming 650034, China

Correspondence: Hao Wu (wuhao@cuit.edu.cn)

Abstract. Temperature inversions (TIs) strongly regulate the accumulation and dispersion of air pollutants, yet their nationwide impacts on surface PM_{2.5} remain poorly quantified. Here we integrate high-resolution L-band radiosonde profiles with PM_{2.5} monitoring data from 2016–2021 to characterize the frequency, intensity, thickness, and diurnal variability of TIs—including surface-based inversions (SBIs) and elevated inversions (EIs)—across mainland China. We show that TIs are pervasive, occurring on average 52% of days, with mean strength of 2.1 °C and thickness of 214 m, and are more common at 08:00 than 20:00. Distinct regional patterns emerge: SBIs dominate in northern China and are significantly stronger 1.3 °C higher than EIs, whereas EIs prevail in eastern China. ~~Distinct regional patterns emerge: SBIs dominate in northern China and are 1.3 °C stronger than EIs, whereas EIs prevail in the east and are 16 m thicker.~~ TIs intensify seasonal pollution, with 76% of PM_{2.5} episodes coinciding with inversion events. SBI strength correlates positively with PM_{2.5} concentrations nationwide, while EI parameters show negative associations in eastern and southern regions. These findings reveal the spatiotemporal dynamics of TIs, establish quantitative links to surface pollution, and highlight regionally divergent mechanisms, providing critical insight for air-quality forecasting and targeted emission control.

Keywords: Temperature inversion, PM_{2.5}, Air pollution, Radiosonde profiles.

1 Introduction

Fine particulate matter (PM_{2.5}, aerodynamic diameter $\leq 2.5 \mu\text{m}$) is a dominant component of atmospheric aerosols and a key indicator and a primary pollutant ~~a major driver~~ of air pollution in China (Liang et al., 2021; Luo et al., 2024; Yan et al., 2023; Zang et al., 2021). Over the past two decades, recurrent severe haze episodes characterized by elevated PM_{2.5} levels have imposed substantial public health burdens, including respiratory, cardiovascular, and reproductive impairments, as well as

31 increased cancer risk (Chan and Yao, [2008](#); Yan et al., [2021](#); Garcia et al., [2023](#); Rentschler and Leonova, [2023](#); Zuo et al.,
32 [2023](#); Chen et al., [2025](#)). In response, stringent emission control policies since 2013 have markedly improved air quality, with
33 annual mean PM_{2.5} concentrations declining from 68 µg m⁻³ in 2013 to 29 µg m⁻³ in 2022 (Meng et al., [2023](#); Peng et al., [2025](#);
34 Zou et al., [2025](#)). Nevertheless, seasonal pollution episodes remain acute, particularly in the Beijing–Tianjin–Hebei (BTH)
35 region, where the 2022 annual mean still reached 44 µg m⁻³ (Ministry of ecology and environment the people’s republic of
36 China, [2022](#)), exceeding the World Health Organization’s Stage-1 interim target of 35 µgm⁻³ (WHO, [2021](#)). Growing evidence
37 shows that such extreme events are not solely determined by anthropogenic emissions but are strongly modulated by adverse
38 meteorological conditions, among which temperature inversion (TI) plays a pivotal role (Feng et al., [2020](#); Morawska et al.,
39 [2021](#); Deng et al., [2022](#); Shao et al., [2023](#); Sun et al., [2025](#)).

40 In meteorology, TI refers to the anomalous increase of temperature with altitude, most frequently observed in the lower
41 troposphere. TIs arise through multiple mechanisms, including nocturnal radiative cooling, warm-air advection, topographic
42 confinement, ~~as well as under specific synoptic conditions such as stationary high-pressure systems (subsidence warming) and~~
43 ~~frontal zones. and subsidence warming under high pressure system~~ (Vihma et al., [2011](#); Kassomenos et al., [2014](#); Largeron
44 and Staquet, [2016](#); Xu et al., [2019](#)). Surface-based inversions (SBIs) typically form at night when radiative cooling produces
45 a shallow, stable layer of cold air near the surface, which usually dissipates after sunrise or under strong winds (>20 km h⁻¹)
46 (Czarnecka et al., 2019). ~~In contrast, elevated inversions (EIs) are often associated with synoptic-scale phenomena. Key driving~~
47 ~~mechanisms include synoptic-scale warm advection, subsidence within high-pressure systems, and frontal overrunning. In~~
48 ~~contrast, elevated inversions (EIs) are driven by synoptic-scale processes such as warm advection over cooler surfaces,~~
49 ~~subsidence within anticyclonic systems, or frontal overrunning~~ (Huang et al., 2021; Palarz et al., 2018).

50 The presence of a temperature inversion (TI) suppresses turbulent mixing, strengthens atmospheric stability, and traps
51 pollutants near the surface (Kahl, [1990](#); Zhong et al., [2018](#)). Within the boundary layer, this stable stratification creates a
52 pronounced “capping effect” that critically limits vertical pollutant dispersion (Stull, [1988](#)). ~~The resulting suppression of~~
53 ~~atmospheric pollutant dispersion and transport operates through three interconnected mechanisms~~ ~~The resulting suppression~~
54 ~~of pollutant ventilation (i.e., the combined cleansing by vertical dispersion and horizontal transport) operates through three~~
55 ~~interconnected mechanisms~~. First, the inversion layer itself acts as a meteorological cap, inhibiting vertical mixing and
56 fostering rapid near-surface accumulation of aerosols (Zhong et al., [2017](#)). Second, synoptic conditions conducive to inversion
57 formation—particularly for surface-based inversions—are often accompanied by weak horizontal winds, further restricting
58 advective transport (Yang and Shao, [2021](#)). Third, the persistence of inversions, especially under wintertime high-pressure
59 systems, prolongs pollution episodes over multiple days, allowing progressive buildup of PM_{2.5} and compounding air quality
60 deterioration (Feng et al., [2020](#)). Collectively, these processes establish TIs as a pivotal meteorological driver of severe
61 pollution across diverse regions.

62 Extensive research over the past two decades has examined the characteristics of temperature inversions (TIs) and their

63 interactions with air pollution (Rendón et al., [2015](#); Wolf et al., [2014](#); Wu et al., [2014](#); Yin et al., [2021](#)). Early studies highlighted
64 their synoptic controls: Milionis and Davies ([1992](#)) identified upper-level inversions between 950–800 hPa over Hemsby, UK,
65 primarily associated with subsidence within anticyclonic systems. At a continental scale, Zhang et al. ([2011](#)) analyzed
66 radiosonde data from 50 U.S. stations and showed that lower-tropospheric inversions (LTIs) are widespread, with strong zonal
67 wind shear playing a key role in their formation. More recently, advanced remote sensing has enabled quantitative assessment
68 of inversion–aerosol interactions. For example, Liu et al. ([2022](#)) combined lidar and radiosonde measurements over the
69 Southern Great Plains to demonstrate that inversion intensity critically determines the aerosol-trapping capacity of the
70 boundary layer.

71 Nonetheless, most existing studies remain limited to individual cities or specific regions. For example, Wallace et al.
72 ([2009](#)) showed that nocturnal inversions in Hamilton, Canada increased PM_{2.5} concentrations by 54%, with mobile
73 observations further revealing the reinforcing role of local topography in inversion formation and pollutant buildup. In China,
74 Xu et al. ([2019](#)) reported that 93% of heavy pollution episodes in Beijing coincided with inversion conditions, while Feng et
75 al. ([2020](#)) found that winter inversions in the Sichuan Basin elevated PM_{2.5} levels by 64.7% compared with non-inversion days.
76 Beyond China, Lagmiri and Dahech ([2024](#)) identified inversions as the dominant driver of particulate pollution in Cergy-
77 Pontoise, France, with nearly 80% of PM₁₀ exceedances occurring under inversion conditions persisting 1–3 days in winter.
78 Structural analyses have also revealed multi-layer inversion systems: Li et al. ([2012](#)) described a four-tiered inversion structure
79 over central China, linking mid-tropospheric inversions to synoptic cold fronts and regional advection, while upper-level
80 inversions exhibited strong latitudinal dependence.

81 While these studies underscore the critical role of inversions in pollution accumulation, substantial knowledge gaps
82 remain regarding their nationwide patterns and interactions with PM_{2.5} across China’s diverse climatic and topographic settings.
83 The country’s complex geography—spanning plains, basins, and plateaus—produces pronounced regional heterogeneity in
84 inversion mechanisms and vertical structures (Yang et al., [2025](#)). For instance, the North China Plain is frequently subjected
85 to strong wintertime SBIs, whereas the Sichuan Basin is characterized by deep, persistent inversions confined by topography
86 (Guo et al., [2020](#); Huang et al., [2021](#); Xu et al., [2021](#)). Such spatial variability drives region-specific impacts on PM_{2.5}
87 accumulation, underscoring the need for systematic, high-resolution observational analyses. Although Yang and Shao ([2021](#))
88 documented a nationwide increase in inversion frequency over the past three decades using reanalysis products, the coarse
89 vertical resolution of datasets such as ERA5 (25 hPa layers) hampers accurate representation of inversion structure. Similarly,
90 radiosonde-based studies (Guo et al., [2020](#); Huang et al., [2021](#); Xu et al., [2021](#)) have provided valuable regional insights but
91 fall short of offering a comprehensive national-scale assessment of boundary-layer inversions and their impacts on PM_{2.5}
92 pollution.

93 In this study, we employ high–vertical-resolution radiosonde observations (6–8 m) from 2016 to 2021 to accurately detect
94 inversion layers and their vertical structures, thereby overcoming the coarse limitations of reanalysis data. By integrating these

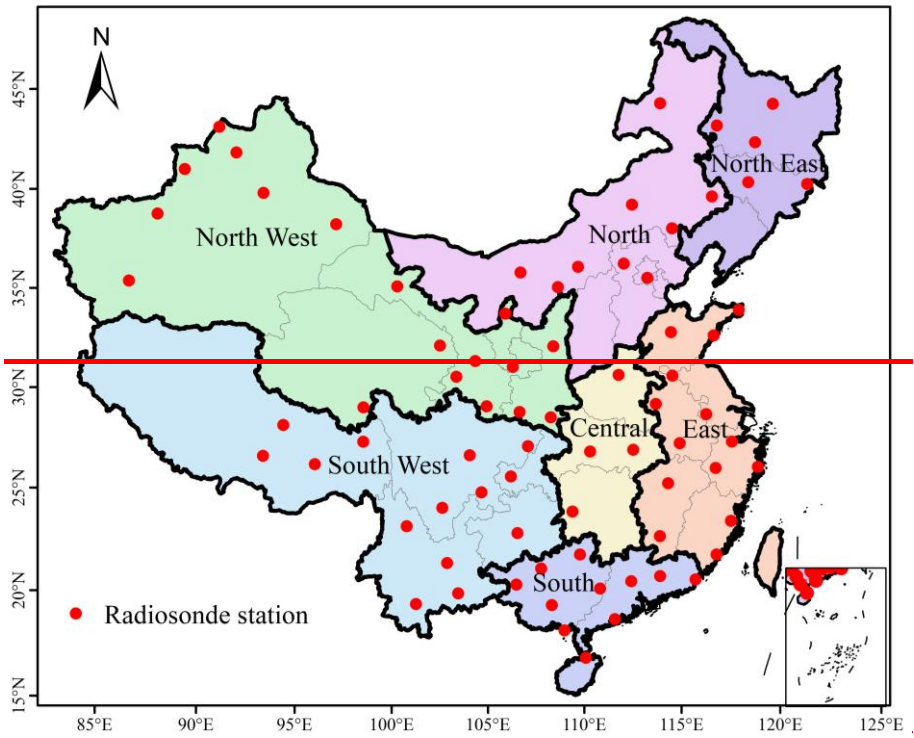
95 measurements with nationwide PM_{2.5} monitoring records from the Ministry of Ecology and Environment, we systematically
96 characterize the spatiotemporal distribution of temperature inversions across China, quantify the distinct impacts of SBI and
97 EI on surface PM_{2.5} concentrations, and establish dynamic relationships between inversion parameters and pollution levels.
98 These findings provide new mechanistic insight into inversion–pollution interactions and offer scientific support for region-
99 specific air quality forecasting and management.

100

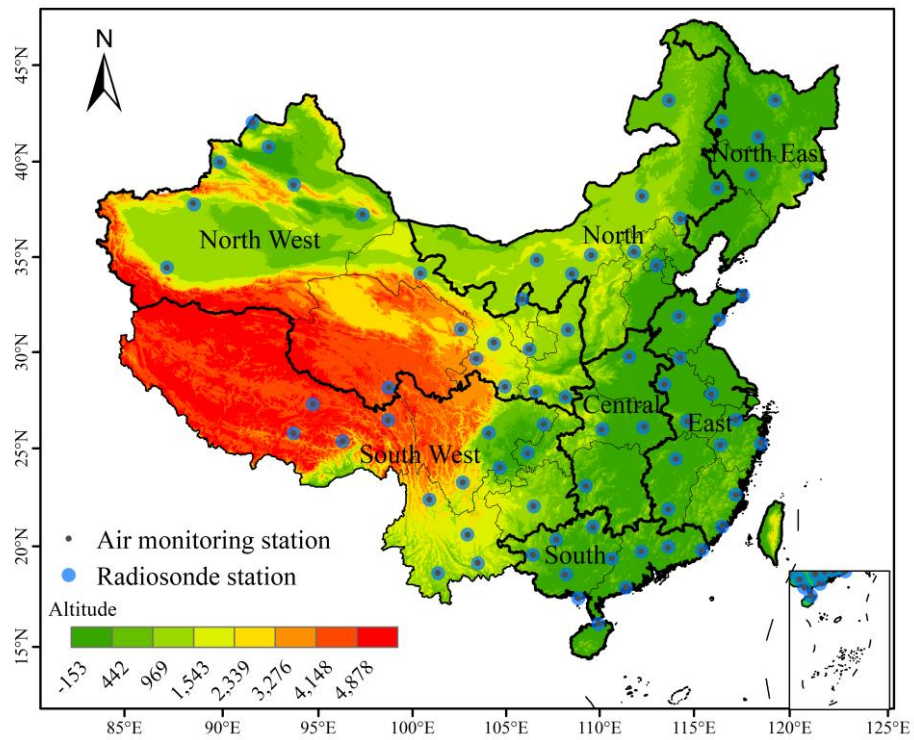
101 **2 Study area and Data**

102 **2.1 Study area**

103 Our analysis covers mainland China, a region of vast spatial extent and pronounced physiographic complexity where
104 monsoonal and continental regimes interact to produce strong environmental heterogeneity. To capture this diversity, we
105 partition the domain (excluding Hong Kong, Macau, and Taiwan owing to data limitations) into seven regions based on
106 standard administrative divisions, integrated meteorological characteristics and major urban agglomerations (Fig. 1). The
107 Northeast (NE)—a traditional industrial base with cold, dry winters—features emissions dominated by coal-fired heating and
108 heavy industry. North China (NC), including the Beijing–Tianjin–Hebei megacity cluster, is characterized by dense population,
109 intensive industrial and vehicular activity, and frequent severe haze. The Northwest (NW) comprises plateaus, basins, and
110 deserts under a continental climate with strong insolation and large diurnal temperature ranges; dust and energy/chemical
111 sectors are major contributors. East China (EC) and South China (SC) lie in the East Asian monsoon zone and are among the
112 most economically active regions, influenced by industrial and traffic emissions and regional transport. Central China (CC),
113 located in the heart of the country, experiences a transitional monsoon climate between the northern subtropical and warm
114 temperate zones, characterized by a terrain dominated by plains and hills. Pollutants tend to accumulate in basins such as the
115 Jiangnan–Dongting Basin due to the region’s enclosed topography and stable atmospheric conditions, where they further
116 combine with polluted air masses transported from the north, resulting in regional and complex air pollution. –The Southwest
117 (SW)—spanning the Tibetan Plateau, the Yunnan–Guizhou Plateau, and the Sichuan Basin—is the most topographically and
118 climatically diverse, where topographic confinement and local circulations strongly modulate pollution composition and
119 evolution.



120



121

122 Fig.1 Distribution of 75 radiosonde stations in China. The inset map in the lower right shows the South China Sea Islands.

123

2.2 Data

124

124 Radiosonde observations. We use L-band high-resolution sounding data from the operational network of the China
 125 Meteorological Administration (CMA). Since nationwide deployment in 2011, the system has routinely operated ~120
 126 radiosonde stations with standard launches at 08:00 and 20:00 Beijing Time (00:00 and 12:00 UTC), with additional warm-

127 season soundings (May–August) to capture monsoon processes (Guo et al., [2016](#); Yan et al., [2020](#)). The GTS1 digital
128 radiosonde provides vertical profiles of temperature, pressure, humidity, wind speed, and direction from the surface (0 m AGL)
129 to ~30 km, with 5–8 m nominal vertical resolution (sampling frequency 1.2 s). By integrating in-situ observations from the
130 co-located surface weather station as the initial record, the valid bottom height for all profiles is strictly maintained at 0 m. The
131 ~~GTS1 digital radiosonde provides vertical profiles of temperature, pressure, humidity, wind speed and direction from the~~
132 ~~surface to ~30 km, with 5–8 m nominal vertical resolution (sampling frequency 1.2 s).~~ Independent assessments indicate
133 temperature errors <0.1 K in the troposphere and data quality comparable to internationally recognized radiosondes within the
134 planetary boundary layer (Ma et al., [2010](#)). These measurements have been widely applied to studies of cloud microphysics,
135 PBL height, and inversion detection, and as inputs to numerical weather prediction and atmospheric composition research (Li
136 et al., [2019](#); Zang et al., [2017](#); Zhang et al., [2020](#)). For this study (2016–2021), we applied routine quality control to remove
137 obvious temperature/height outliers and used the full-resolution vertical profiles to identify inversion layers and derive their
138 properties.

139 Surface PM_{2.5} monitoring. Hourly PM_{2.5} concentrations were obtained from the national air-quality monitoring network
140 operated by the China National Environmental Monitoring Centre (CNEMC; real-time platform: <https://www.cnemc.cn/en/>)
141 (Miao et al., [2020](#); Yan et al., [2020](#)). As of 1 March 2022, the network comprised 2,026 stations with dense coverage in
142 eastern urban clusters and relatively sparse representation in western high-altitude regions. To match radiosonde stations
143 with PM_{2.5} monitors, we used a distance threshold method with a 10 km search radius. This approach identified 75 valid
144 station pairs, balancing spatial representativeness and sample size (Fig. 1). The 10 km threshold avoids underrepresentation
145 from smaller radii and minimizes spatial error from larger distances, representing the point where further increases yield
146 diminishing returns in matches (the distribution of original sites and the screening method are referenced in Figs S1 and
147 S2, the specific screening method is shown in Fig. S1). For temporal alignment with the soundings, hourly PM_{2.5} records
148 were extracted around 08:00 and 20:00 BJT. Basic completeness checks and standard plausibility screening were applied
149 before analysis.

150 Rationale for integration. The combination of meter-scale-resolution vertical thermodynamic profiles with collocated
151 surface PM_{2.5} enables a consistent, observation-based assessment of inversion frequency, intensity, and thickness—and their
152 diurnal and regional variability—while overcoming the coarse vertical structure inherent in reanalysis products (Li et al., [2019](#);
153 Yan et al., [2020](#); Zhang et al., [2020](#))

154 **3 Method**

155 The sounding data underwent manual quality control to identify and systematically remove obvious errors in temperature and
156 height measurements. Raw temperature profiles were first interpolated using cubic splines to ensure vertical continuity. TIs

157 were then identified by applying a first-derivative algorithm to the smoothed profiles (Kahl, 1990; Serreze et al., 1992). Each
 158 profile was scanned upward from the surface; layers exhibiting a positive vertical temperature gradient were classified as
 159 inversion layers, while those with negative gradients were considered non-inversion zones. The base height of an inversion
 160 layer was defined as the lowest altitude at which temperature began to increase with height, and the top height was identified
 161 as the point where the gradient reverted to negative. Following Kahl et al. (1996), three fundamental TI parameters were
 162 derived: inversion thickness (ΔH), inversion strength (ΔT), inversion frequency (F_{TI}). They are defined as:

$$163 \quad \Delta H = H_t - H_b \quad (1)$$

$$164 \quad \Delta T = T_t - T_b \quad (2)$$

$$165 \quad F_{TI} = N_{TI}/N \quad (3)$$

$$166 \quad F_{SBI} = N_{SBI}/N \quad (4)$$

$$167 \quad F_{EI} = N_{EI}/N \quad (5)$$

168 where H_t and H_b represent the top and bottom heights of the temperature inversion layer respectively; T_t and T_b represent
 169 the temperatures at the top and bottom respectively; N represents the total number of detections, N_{TI} represents the number
 170 of detections where temperature inversion occurs, and N_{SBI} and N_{EI} represent the number of detections where SBI and EI
 171 occur respectively.

172 To mitigate false positives from small-scale turbulence (e.g., "sawtooth" noise in balloon-borne measurements),
 173 thresholds for ΔH and ΔT were imposed per established practices (Guo et al., 2020; Kahl, 1990). A layer was classified as
 174 a valid TI only if $\Delta H \geq 100$ m and $\Delta T \geq 0.5^\circ\text{C}$; otherwise, it was discarded. Non-inversion layers embedded within broader
 175 TIs were permitted, provided the overarching TI met these criteria. The temperature profile was scanned upward from the
 176 surface, and the first continuous layer satisfying $\Delta H \geq 100$ m and $\Delta T \geq 0.5^\circ\text{C}$ was identified as the inversion for that
 177 sounding. To specifically target thermodynamic processes influencing surface air quality, this study considers only inversion
 178 layers with a base height $H_b \leq 2000$ m. Inversion can also be classified into SBI and EI based on the base height. When H_b
 179 < 100 m, it is called Surface-based inversions (SBIs); when $100 \text{ m} < H_b \leq 2000 \text{ m}$, it is called Elevated inversions (EIs).
 180 (For additional validation at different thickness thresholds, please refer to supplementary Figures S18-S20.)—Theoretical
 181 calculations indicate that each station should have a total of 4384 soundings at 12-hour intervals from 2016 to 2021. In practice,
 182 however, data omissions occurred due to various factors, resulting in an average missing rate of 3.2% for temperature inversion
 183 data in the final statistics.

184 According to China's National Ambient Air Quality Standards (GB3095-2012), the standard for a pollution event is based
 185 on a daily mean $\text{PM}_{2.5}$ concentration exceeding $75 \mu\text{g m}^{-3}$. In this study, to align with the instantaneous radiosonde observations
 186 at 08:00 and 20:00 BJT, we applied this concentration threshold $75 \mu\text{g m}^{-3}$ to the hourly $\text{PM}_{2.5}$ data to identify pollution events
 187 corresponding to the sounding times.~~According to China's National Ambient Air Quality Standards (GB3095-2012), a~~
 188 ~~pollution event is defined when the $\text{PM}_{2.5}$ concentration exceeds $75 \mu\text{g m}^{-3}$.~~ $\text{PM}_{2.5}$ concentrations are further classified into six

189 categories: Excellent: 0-35 $\mu\text{g m}^{-3}$; Good: 35-75 $\mu\text{g m}^{-3}$; Light pollution: 75-115 $\mu\text{g m}^{-3}$; Moderate pollution: 115-150 $\mu\text{g m}^{-3}$;
190 Severe pollution: 150-250 $\mu\text{g m}^{-3}$; Extreme pollution: >250 $\mu\text{g m}^{-3}$. To align with the spatiotemporal characteristics of the
191 radiosonde data, the hourly $\text{PM}_{2.5}$ data were processed into two time periods corresponding to the radiosonde observations:
192 08:00 and 20:00 Beijing Time.

193 4 Results and Discussions

194 4.1 Spatiotemporal distribution of atmospheric temperature inversions in China

195 The base height of TI sets the effective lid for vertical pollutant dispersion. To resolve its vertical structure within the boundary
196 layer, we quantified the vertical distribution of inversion events. This is defined as the percentage of the total number of
197 inversion events falling within each 100-m height bin from the surface to 2 km (Fig. 2). A distinct non-linear profile emerges:
198 The TI proportion peaks sharply in the lowest 0–100 m bin, which comprises exclusively SBIs and accounts for 22.2% of all
199 inversion events. This peak is followed by a rapid decline to a minimum of 3.1% at 600–700 m, and then a gradual recovery
200 to 5.1% at 1800–1900 m—i.e., a “rapid decline, then slow recovery” with height.

201 ~~The base height of a temperature inversion (TI) sets the effective lid for vertical pollutant dispersion. To resolve its vertical~~
202 ~~structure within the boundary layer, we quantified the vertical distribution of inversion events. This is defined as the percentage~~
203 ~~of the total number of inversion events falling within each 200 m height bin from the surface to 2 km (Fig. 2). A distinct non-~~
204 ~~linear profile emerges: TI proportion peaks at 27.5% near the surface (0–200 m), declines sharply to a minimum of 6.4% at~~
205 ~~600–800 m, and then gradually increases to 10.0% at 1,800–2,000 m—i.e., a “rapid decline, then slow recovery” with height.~~

206 Marked regional contrasts accompany this vertical pattern. In the near-surface layer (0–100 m, i.e., the SBI), the Northwest
207 exhibits the highest TI proportion 31.6%, followed by Southwest 30.5%. In comparison, Central, East, and South China show
208 lower near-surface SBI proportions, with South China the lowest 9.8%. The pattern reverses aloft: for elevated inversions in
209 the 1000–2000 m layer, South China records the highest proportion 56.0%, whereas northern regions are much less affected.
210 Taken together, intense near-surface trapping by SBIs preferentially occurs over inland northern and southwestern China, while
211 EIs are more common and reach higher altitudes in the southeastern coastal belt. A potential driver of this dipole is the diurnal
212 temperature range (DTR): larger DTRs over inland regions enhance nocturnal radiative cooling, favoring strong SBIs; weaker
213 DTRs in maritime-influenced southeastern areas favor synoptic processes that produce EIs.”

214 ~~Marked regional contrasts accompany this vertical pattern. In the near-surface layer (0–200 m), the Southwest exhibits the~~
215 ~~highest TI proportion (36.0%), followed by northern regions—Northeast, North, and Northwest China (mean 34.7%). In~~
216 ~~comparison, Central, East, and South China show lower near-surface inversion proportion, with South China the lowest~~
217 ~~(14.1%). The pattern reverses aloft: for elevated inversions (1,800–2,000 m), South China records the highest proportion~~
218 ~~(12.5%), whereas northern regions are much less affected, reaching a minimum in North China (7.0%). Taken together, near-~~

surface inversions preferentially occur over inland northern and southwestern China, while elevated inversions are more common in the southeastern coastal belt. A plausible driver of this dipole is the diurnal temperature range (DTR): larger DTRs over inland northern and southwestern regions enhance nocturnal radiative cooling, favoring shallow, surface-based inversions; weaker DTRs in maritime-influenced southeastern areas favor synoptic processes that produce elevated inversions.

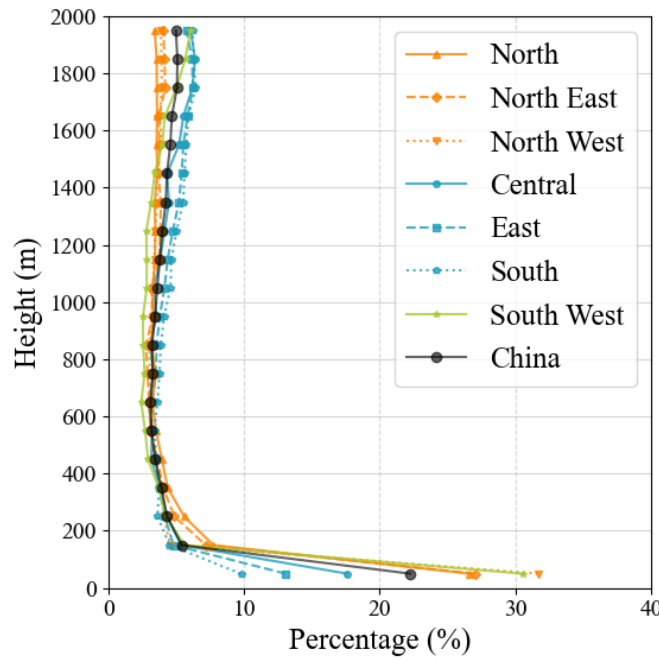
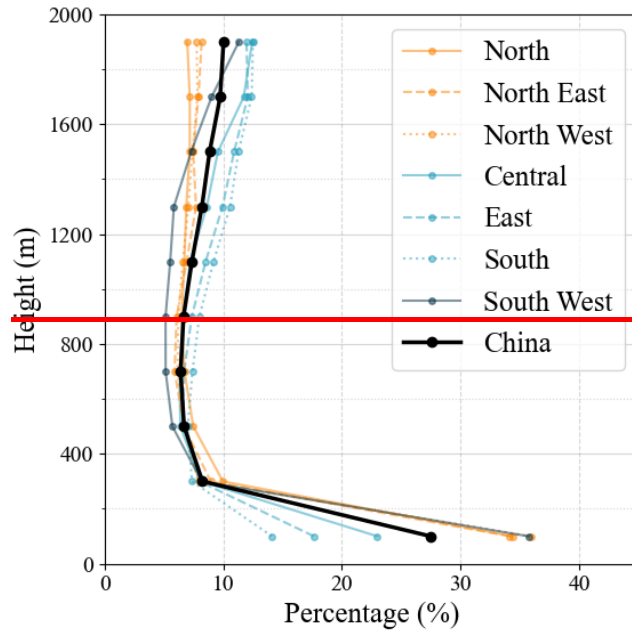


Fig.2 Vertical distribution of inversion base height: fraction of total inversions per height bin.

4.1.1 Inversion frequency

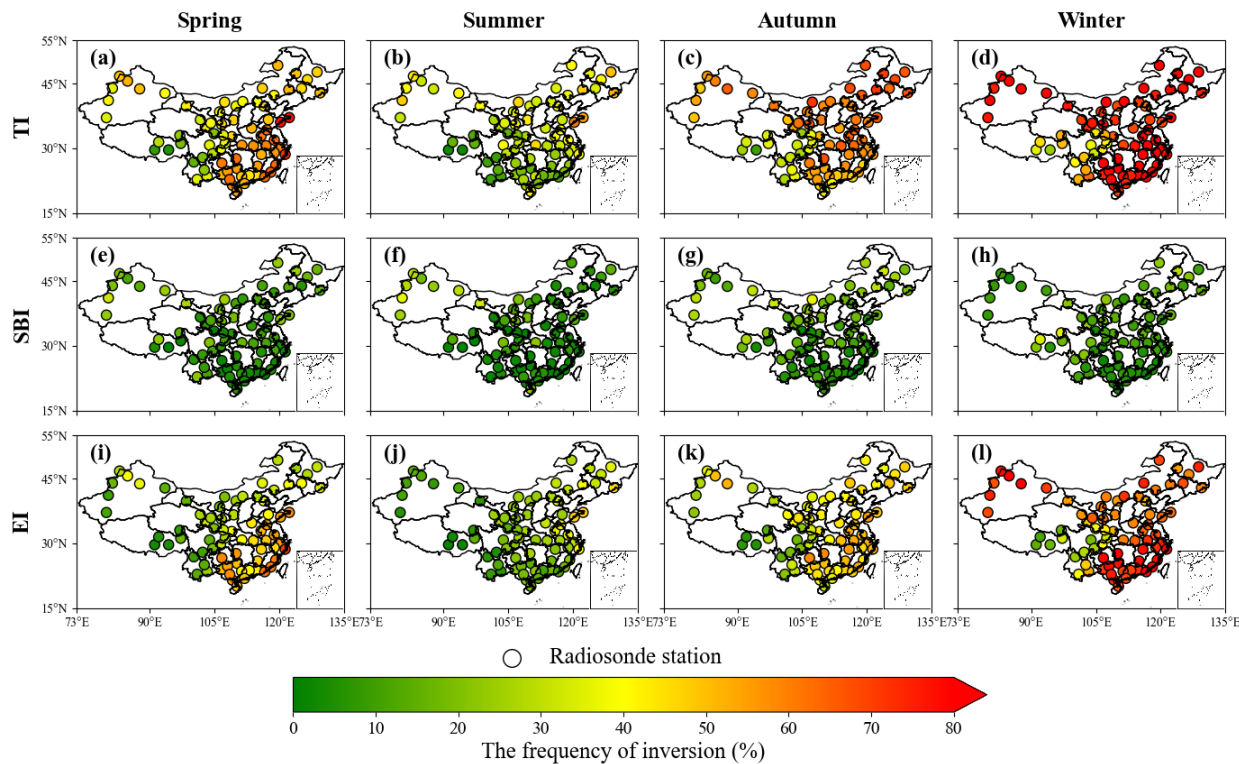
Figure 3 maps the spatial and seasonal variability of TI frequency over China (2016–2021), revealing pronounced regional

230 heterogeneity. High TI occurrence is concentrated along the coasts (East and South China) and across northern China
231 (Northeast, North, Northwest), yielding a national annual mean of 54.9%. ~~Regionally, Northeast China records the highest~~
232 ~~frequency (59.5%), whereas the Southwest exhibits the lowest (31.3%; Table 1)~~ ~~Northeast China records the highest frequency~~
233 ~~(59.5%), whereas the Southwest is lowest (31.3%; Table 1)~~. The suppressed occurrence in the Southwest likely reflects two
234 factors: (i) ~~in the Sichuan Basin, the dominant signal is lower-tropospheric inversions (LTIs) which typically occur at altitudes~~
235 ~~of 2,200–3,400 m—well above the 0–2,000 m height range examined in this study—resulting in their exclusion from our~~
236 ~~frequency statistics~~ ~~in the Sichuan Basin the dominant signal is lower tropospheric inversions (LTIs) that often peak above the~~
237 ~~boundary layer depths emphasized here~~, and (ii) plateau climate conditions—high elevation, strong solar radiation, low air
238 density, and frequent strong winds linked to the westerly jet—enhance turbulent mixing and disrupt inversion persistence (Feng
239 et al., 2020; Schiemann et al., 2009). ~~National averages by type indicate SBIs ~13% and EIs ~43% annually (Figs. 4d, 4g).~~
240 ~~Elevated inversions (EIs) dominate total events nationally. The two inversion types exhibit contrasting geography: SBIs cluster~~
241 ~~over northern China (Northeast, North, Northwest) with annual frequencies of 14.9–16.145.8%, whereas EIs prevail across the~~
242 ~~southeastern coastal and central regions (South, East, Central China), averaging 48.1% and peaking at 51.6% in East China.~~
243 ~~This spatial dipole aligns with previous radiosonde climatologies, which report more frequent SBIs in northern/western China~~
244 ~~and EI dominance in the south and east (Huang et al., 2021).~~ ~~A persistent “east-high, west-low” gradient is also evident. One~~
245 ~~contributing factor is the fixed launch time relative to local solar time: China spans roughly five time zones, so the 08:00 BJT~~
246 ~~sounding corresponds to ~05:00 local time in the far west, when nocturnal inversions may not yet have fully developed, biasing~~
247 ~~frequencies lower there.~~

248 Figure 4a shows pronounced seasonality in TI occurrence. The highest monthly means occur at 08:00 BJT in January
249 (84.0%) and at 20:00 BJT in December (68.8%), whereas minima appear in June (31.9%) and August (32.0%). ~~National~~
250 ~~averages by type indicate SBIs ~13% and EIs ~43% annually (Figs. 4d, 4g).~~ ~~SBI occurrence shows relatively high frequencies~~
251 ~~(>24%) in February, March, September, and October, whereas EI frequency exhibits a sharp, single peak in January~~
252 ~~(75.2%). SBI occurrence peaks in February, March, September, and October (all >24%), while EI frequency maximizes in~~
253 ~~January (75.2%).~~ Seasonal contrasts are stark: inversions are most frequent in the cold season and relatively rare in the warm
254 season. The spatial footprint of inversion-prone areas expands westward from summer to winter: in summer, only the Northeast
255 exceeds 40%, and the Southwest falls to 17.5%; in winter, all regions except the Southwest surpass 70%, reaching 80.5% in
256 the Northeast. SBIs and EIs share this seasonal phasing—winter maxima, summer minima—consistent with longer winter
257 nights that enable sustained radiative cooling and stronger stability. ~~A persistent “east high, west low” gradient is also evident.~~
258 ~~One contributing factor is the fixed launch time relative to local solar time: China spans roughly five time zones, so the 08:00~~
259 ~~BJT sounding corresponds to ~05:00 local time in the far west, when nocturnal inversions may not yet have fully developed,~~
260 ~~biasing frequencies lower there.~~

261 Further analysis (Figs. S5?, S6? and 4a)(Figs. S2, 4a) shows a robust dawn–dusk asymmetry: inversions are more likely

262 to occur at 08:00 BJT across all regions and seasons, with daytime launches accounting for 62% of all TI detections. The
 263 contrast is strongest in summer, when 08:00 inversions comprise 71% of events, and weaker in winter (57%). This seasonal
 264 modulation reflects differences in solar forcing. In summer, long days and short nights curtail both the formation window and
 265 stability of inversions: with sunrise near 05:20 BJT, 2–3 hours of insolation have already eroded the nocturnal layer by 08:00,
 266 and by 20:00 roughly 12 hours of high-angle solar heating have largely dissipated residual stability—yielding a 26.4%
 267 frequency gap between the two launch times. In winter, short days and long nights promote the development of deeper and
 268 more persistent inversions through enhanced radiative cooling. With sunrise as late as around 07:20 BJT, the weak early-
 269 morning insolation preceding the 08:00 sounding is insufficient to dissipate the TI layer significantly. Furthermore, the
 270 wintertime atmosphere is significantly drier (Fig. S7), which minimizes downward longwave radiation and thereby maximizes
 271 the efficiency of nocturnal surface cooling. The subsequent ~10 hours of low-angle daylight provide insufficient thermal energy
 272 to significantly disturb the stable surface layer before 20:00. Consequently, the 08:00–20:00 frequency difference contracts to
 273 14.8% in winter. In winter, short days and long nights promote deeper, more persistent inversions: with sunrise around 07:20
 274 BJT, less than an hour of weak insolation precedes the 08:00 sounding, and the subsequent ~10 hours of low-angle daylight
 275 only modestly disturb the surface layer before 20:00. Consequently, the 08:00–20:00 difference contracts to 14.8% in winter.
 276



277
 278 Fig. 3. Spatial and seasonal distribution of occurrence frequency for different types of TI. For more details about SBI, please refer to Fig.

279 S15.

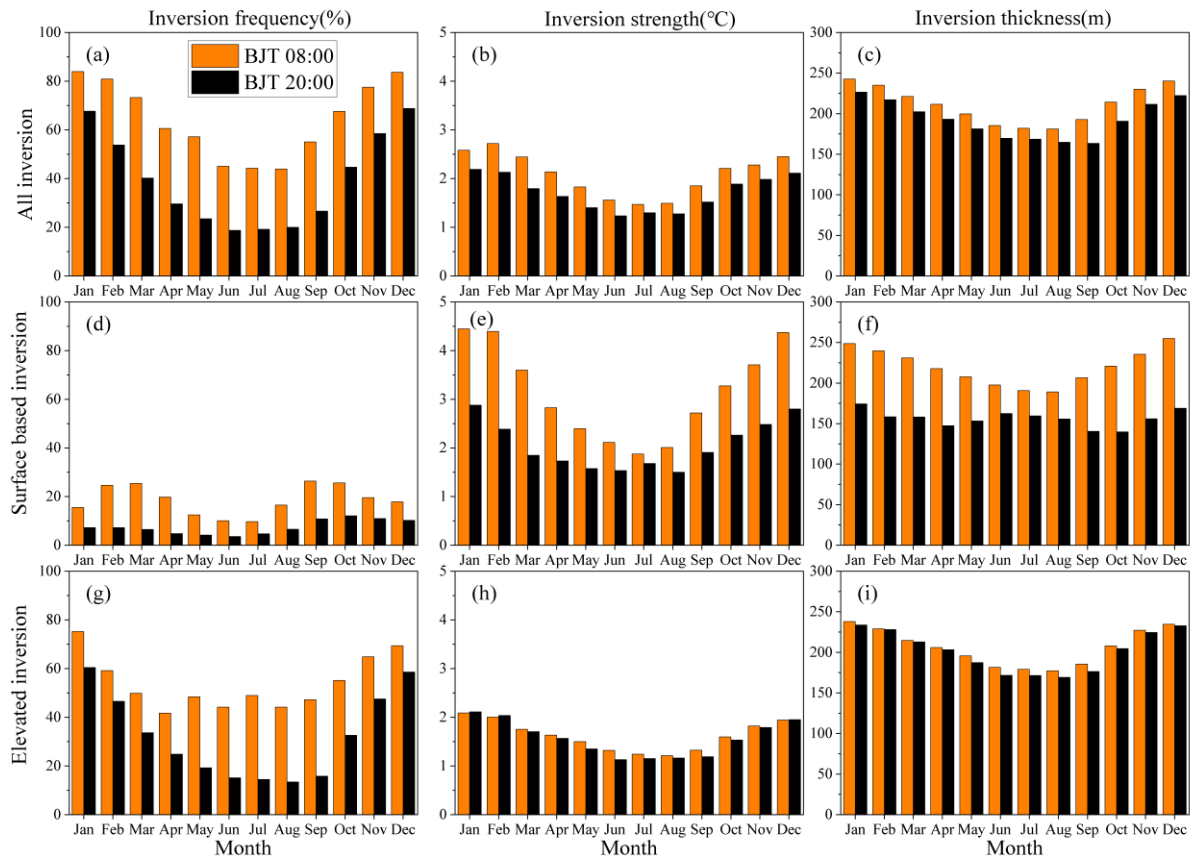


Fig. 4 Monthly variations of TI parameters in China (2016–2021).

Table 1. Annual mean values of TI parameters by region.

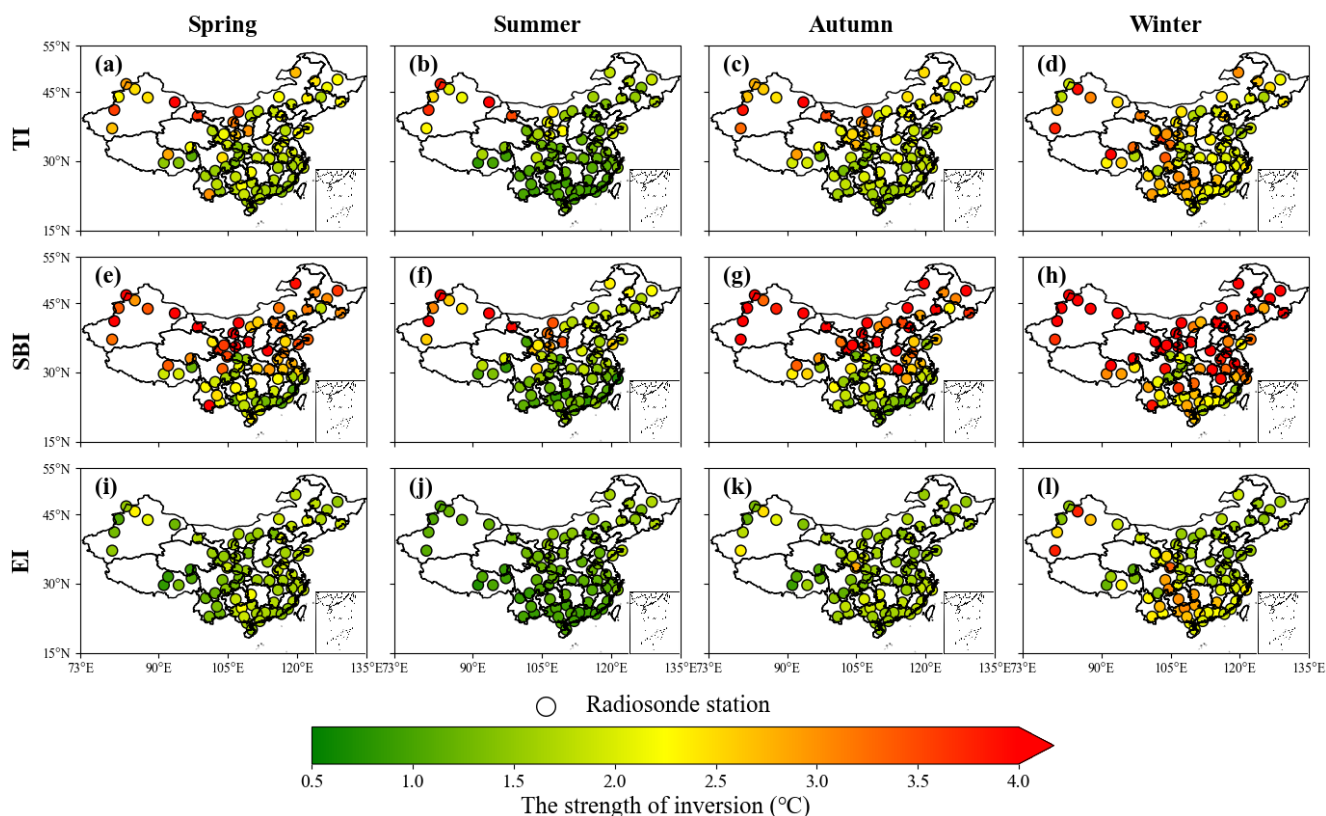
| Region | TI | | | SBI | | | EI | | |
|------------|--------------|------------------------------|----------------------|---------------|------------------------------|----------------------|--------------|------------------------------|----------------------|
| | $F_{TI}(\%)$ | $\Delta T(^{\circ}\text{C})$ | $\Delta H(\text{m})$ | $F_{SBI}(\%)$ | $\Delta T(^{\circ}\text{C})$ | $\Delta H(\text{m})$ | $F_{EI}(\%)$ | $\Delta T(^{\circ}\text{C})$ | $\Delta H(\text{m})$ |
| Central | 57.0 | 2.08 | 231 | 10.0 | 3.54 | 213 | 47.0 | 1.80 | 235 |
| East | 59.3 | 1.86 | 217 | 7.7 | 2.54 | 197 | 51.6 | 1.74 | 219 |
| North | 55.8 | 2.20 | 201 | 14.9 | 3.72 | 204 | 40.9 | 1.63 | 199 |
| North East | 59.5 | 2.11 | 211 | 16.1 | 3.34 | 210 | 43.4 | 1.63 | 212 |
| North West | 49.3 | 2.67 | 215 | 15.8 | 3.91 | 209 | 33.5 | 1.92 | 218 |
| South | 50.7 | 1.92 | 222 | 5.0 | 1.74 | 186 | 45.7 | 1.93 | 227 |
| South West | 31.3 | 2.05 | 202 | 9.6 | 2.39 | 186 | 21.7 | 1.66 | 202 |

4.1.2 Inversion strength

Among the key TI parameters, strength exerts first-order control on pollutant dispersion. The TI exerts first-order control on

291 **pollutant dispersion**. Spatially, TI strength is greater over inland northern regions than over southern and eastern coasts (Fig.
 292 5; Table 1): the Northwest has the highest annual mean (2.67 °C), whereas the East is lowest (1.86 °C). Extremes span 4.69 °C
 293 in the Southwest to 1.67 °C in the East. Seasonally, TI strength peaks in winter (2.44 °C), weakens in spring and autumn (both
 294 ~2.10 °C), and is lowest in summer (1.53 °C) (Fig. 5). Monthly values maximize in February (2.73 °C) and minimize in June
 295 (1.23 °C) (Fig. 4b). By inversion type, SBIs are consistently stronger than EIs: peak intensities reach 4.45 °C (SBI) versus
 296 2.11 °C (EI) (Figs. 4e, 4h). Correspondingly, annual means rank SBI (3.02 °C) > all TI (2.13 °C) > EI (1.76 °C). The strongest
 297 seasonal maxima occur in winter in the Northwest for both overall TI (2.78 °C) and SBI (4.88 °C), while EI intensity peaks in
 298 winter in the South (2.43 °C). Notably, winter SBI strength exceeds EI by more than a factor of two. Geographically, SBI
 299 intensity varies substantially—annual means in northern and northwestern China are over twice those in the south—whereas
 300 EI strength is comparatively uniform, ranging from 1.63 °C (North/Northeast) to 1.93 °C (South), a spread of only 0.30 °C.
 301 Diurnally, TI, SBI, and EI intensities are generally higher at 08:00 BJT than at 20:00 (Figs. 4b, 4e, 4h). EI shows a regional
 302 reversal: daytime-stronger in the Northeast/North, but nighttime-stronger elsewhere. The maximum values by category occur
 303 at 08:00 in the Northwest for all TI (2.81 °C), 08:00 in the North for SBI (4.30 °C), and 20:00 in the South for EI (2.02 °C)
 304 (Tables S21, S32).

305



306

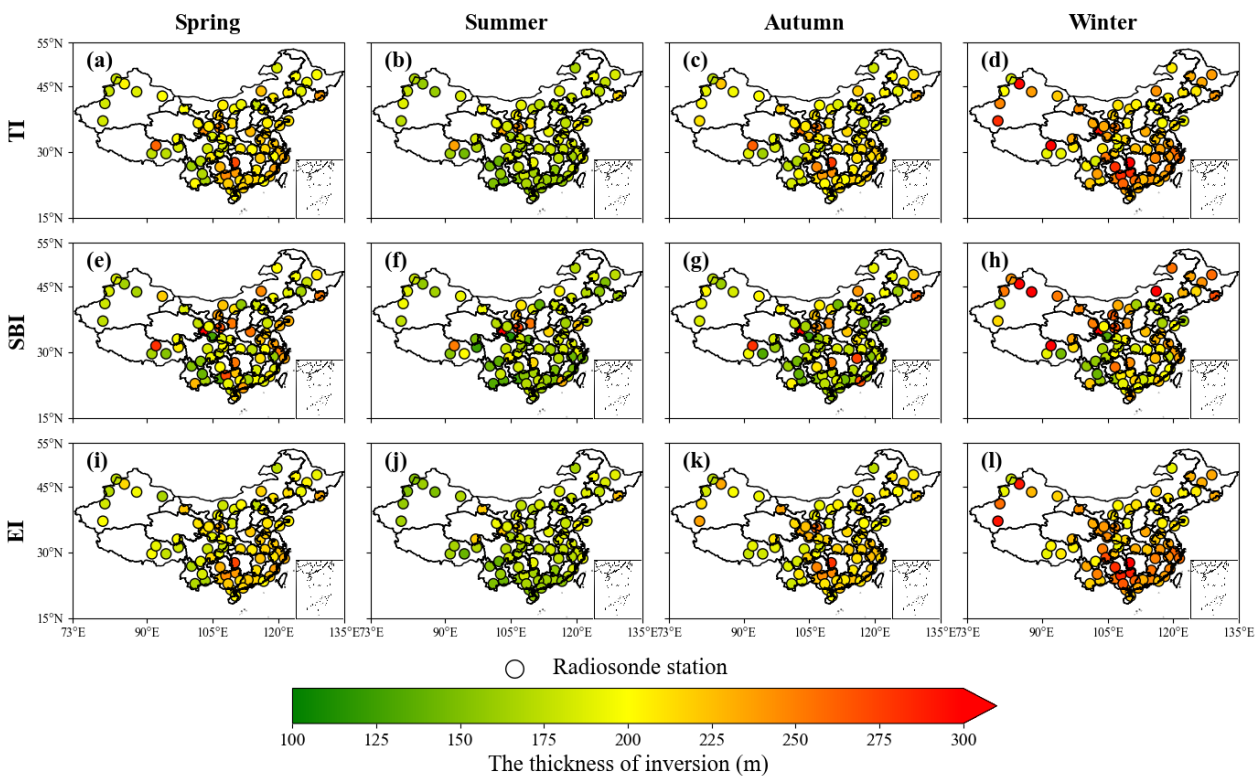
307

Fig.5 Spatial and seasonal distribution of inversion strength for different types of inversions.

308

309 **4.1.3 Inversion thickness**

310 Seasonal and regional patterns of inversion thickness for all TIs, SBIs, and EIs are shown in Figure 6 and summarized in Table
 311 1. Across the 75 radiosonde stations, the annual mean thickness is 214 m. Layers sampled at 08:00 BJT are generally thicker
 312 than those at 20:00 BJT by about 40 m, consistent with the diurnal phasing of inversion intensity. Thickness varies markedly
 313 by season, maximizing in winter (231 m; Fig. 6d) and minimizing in summer (179 m; Fig. 6b). Monthly evolution follows a
 314 pronounced “V” shape (Fig. 4c), with a January peak of 243 m. By type, EIs are systematically thicker than SBIs, with annual
 315 means of 216 m and 201 m, respectively. Both exhibit winter maxima and summer minima. At 08:00, EI and SBI each display
 316 a clear “V”-shaped monthly cycle, whereas at 20:00 their behavior diverges: SBI thickness varies only modestly, while EI
 317 thickness remains comparatively stable across months (Figs. 4f, 4i). Spatially, TIs are notably thicker in the eastern and
 318 southern regions compared to the northern and western inland areas. Specifically, the average thickness in East, South, and
 319 Central China is 223 m, whereas it is 209 m in Northeast, North, and Northwest China. Spatially, inversion layers are thicker
 320 in the east and south—East, South, and Central China average 223 m—than in the north and west—Northeast, North, and
 321 Northwest average 209 m. South China shows the largest annual mean thickness (231 m), exceeding the national mean,
 322 whereas the Southwest has the thinnest layers (202 m). This pattern aligns with the regional predominance of inversion types:
 323 thicker EIs prevail in the eastern/southern regions, while thinner SBIs are more common in the western/northern regions. The
 324 lower overall inversion frequency in the Southwest, combined with the intrinsic thickness contrast between EI and SBI, further
 325 contributes to these regional differences. Additionally, we discussed the scenario where the lapse rate ($\Delta T/\Delta H$) was used as a
 326 proxy for inversion strength, as elaborated in supplementary Fig. S16, S17 and Table. S4.



4.2 The correlation between temperature inversion and PM_{2.5}

4.2.1 Statistical relationship between temperature inversion and PM_{2.5} pollution events

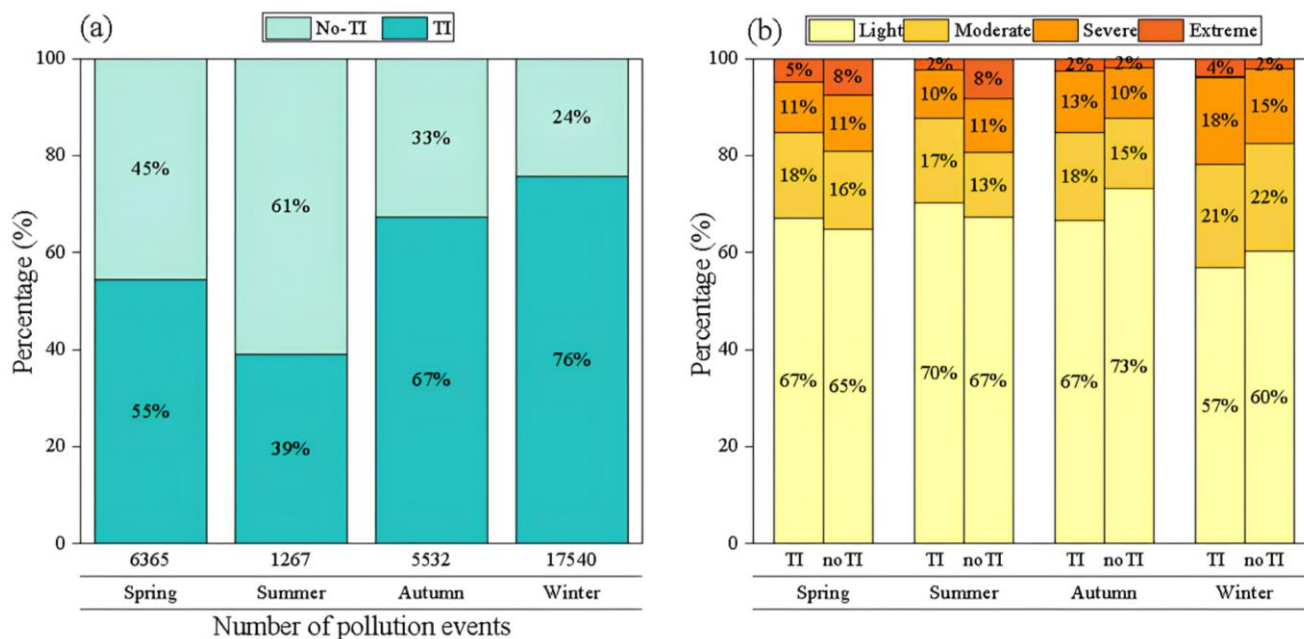
We quantified the linkage between TIs and PM_{2.5} pollution by comparing the share of polluted days under inversion versus non-inversion conditions in each region (Table 2). At 08:00 BJT, a strong association emerges nationwide: co-occurrence rates span 84.6% in the Northeast (NE) to 62.9% in the Southwest (SW), indicating that morning pollution accumulation is substantially conditioned by inversions, with northern regions particularly sensitive—consistent with their higher prevalence of SBIs. By contrast, at 20:00 BJT the TI–PM_{2.5} coupling weakens markedly; the SW shows the lowest overlap, with only 27.7% of pollution events coinciding with inversions. This pronounced diurnal asymmetry suggests distinct formation regimes: daytime/morning pollution is frequently meteorology-limited by inversion trapping, whereas evening pollution is more strongly governed by emission timing and chemical processes than by boundary-layer stability.

Table 2. Frequency statistics of temperature inversion corresponding to PM_{2.5} pollution events in seven regions of China from 2016 to 2021.

| Region | BJT 08:00 | | | | BJT 20:00 | | | |
|------------|-----------|-----------|--------------|----------------------|-----------|-----------|--------------|----------------------|
| | Pollution | Inversion | No-inversion | Inversion proportion | Pollution | Inversion | No-inversion | Inversion proportion |
| Central | 1818 | 1489 | 329 | 81.9% | 1713 | 1027 | 686 | 60.0% |
| East | 3239 | 2672 | 567 | 82.5% | 3004 | 1910 | 1094 | 63.6% |
| North | 1749 | 1394 | 355 | 79.7% | 1433 | 773 | 660 | 53.9% |
| North East | 1072 | 907 | 165 | 84.6% | 709 | 480 | 229 | 67.7% |
| North West | 5409 | 4443 | 966 | 82.1% | 4734 | 2299 | 2435 | 48.6% |
| South | 1194 | 891 | 303 | 74.6% | 881 | 464 | 417 | 52.7% |
| South West | 2523 | 1586 | 937 | 62.9% | 2186 | 608 | 1578 | 27.7% |

Figure 7a reveals strong seasonal heterogeneity. Winter registers the most pollution events (17,540), exceeding spring, autumn, and summer by factors of 2.7, 3.2, and 13.8, respectively. Temperature inversions (TIs) substantially amplify this seasonal contrast: relative to no-inversion conditions, the probability of a pollution event rises by +52% in winter, +34% in autumn, +10% in spring, and is negligible in summer. The muted summer response likely reflects a shift toward ozone-dominated chemistry, weakening the coupling between PM_{2.5} and inversion dynamics. Figure 7b shows that TIs not only increase

349 occurrence but also severity—especially in winter—doubling extreme events (Level 4: 2% → 4%) and raising severe events
 350 (Level 3) by 3 percentage points (15% → 18%). These observations are consistent with the inversion-driven explosive growth
 351 conceptual model for PM_{2.5} (Zhong et al., 2017, 2018) and with the view that extreme haze is tightly linked to inversion
 352 meteorology (Yang and Shao, 2021). Autumn TIs exhibit a similar but weaker intensification (+3% in moderate/severe
 353 categories), whereas spring and summer TIs chiefly affect lower-severity bins. Collectively, the results establish TIs as a critical
 354 wintertime meteorological driver of both the frequency and intensity of haze in China.



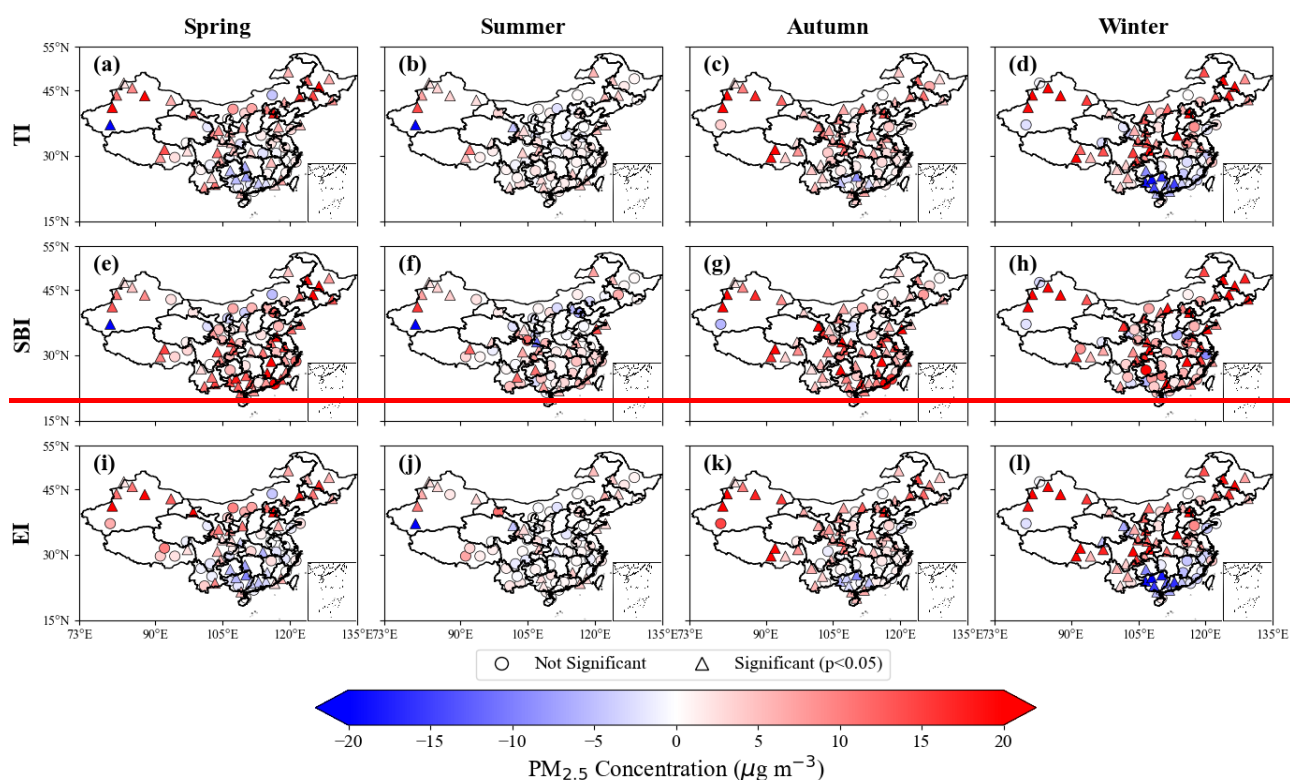
355
 356 Fig. 7 (a) Frequency of inversion occurrence during polluted periods and (b) distribution of pollution levels in China (2016–2021).

357 4.2.2 Impacts of different TI types on PM_{2.5} concentrations

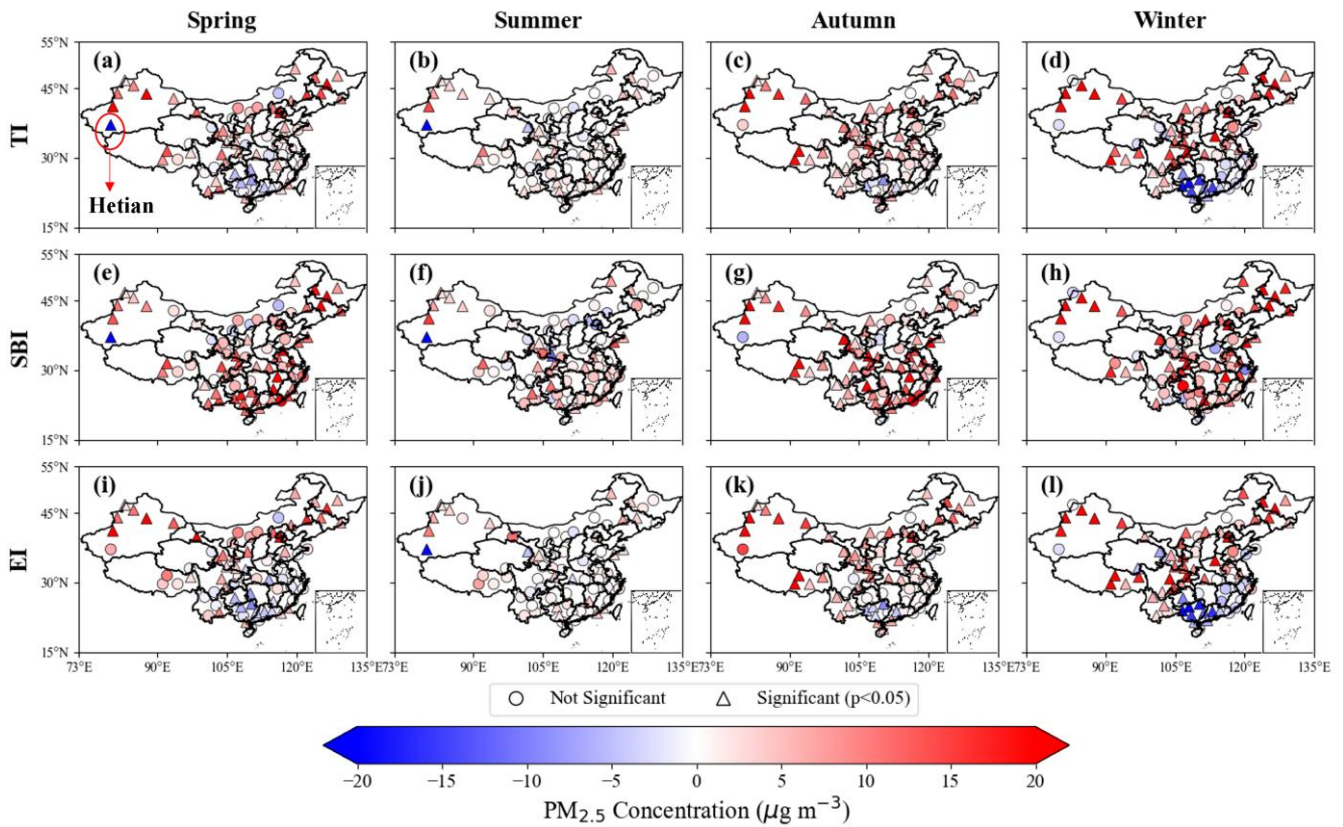
358 We quantify inversion impacts by contrasting the daily mean PM_{2.5} concentrations under inversion and non-inversion
 359 conditions, with statistical significance assessed using two-sample t-tests (Fig. 8). The time-resolved analyses for 08:00 and
 360 20:00 BJT are shown in Figs. S12 and S13. ~~We quantify inversion impacts by contrasting mean PM_{2.5} under inversion and non-~~
 361 ~~inversion conditions and assessing significance with two sample t tests for observations at 08:00 and 20:00 BJT (Fig. 8).~~ In
 362 eastern China, results broadly align with Shao et al. (2023): PM_{2.5} increases significantly under inversions in the Northeast
 363 (NEC) and North China (NC), whereas South China (SC) exhibits significant decreases. In western China, most stations also
 364 show PM_{2.5} enhancements during inversions, with a notable exception at Hetian (southern Xinjiang), where spring–summer
 365 concentrations decline significantly (Figs. 8a, 8b). This anomaly likely reflects the dust-dominated composition of PM_{2.5}
 366 (>90%) and frequent spring–summer dust storms near the Taklamakan Desert; strong winds that accompany dust events are
 367 unfavorable for inversion formation, rendering dust outbreaks and inversion episodes largely mutually exclusive (Aishajiang
 368 et al., 2020). Consequently, during inversion periods, the dominant dust component is largely absent, yielding lower PM_{2.5}.

369 Disaggregating by inversion type reveals fundamentally different mechanisms. Surface-based inversions (SBIs) robustly

370 increase PM_{2.5} across most regions—especially in winter and autumn (Figs. 8g, 8h)—consistent with nocturnal radiative
 371 cooling that produces a shallow, stable layer, suppresses vertical mixing, and accelerates near-surface accumulation (Stull,
 372 1988; Zhong et al., 2017). The amplification in northern winters reflects longer nights and stronger surface cooling. By contrast,
 373 elevated inversions (EIs) exhibit spatially variable effects: they enhance PM_{2.5} in NEC, NC, and Northwest China (NWC), but
 374 reduce concentrations in SC. This pattern supports the hypothesis that EIs can inhibit pollutant transport (Yang and Shao,
 375 2021): in SC, EIs often accompany synoptic subsidence or warm advection, establishing a capping layer that limits vertical
 376 exchange and isolates the region from northerly inflow. Such a transport-suppression mechanism is less relevant in northern
 377 China, where local emissions dominate. Diurnal contrasts further modulate these responses: morning (08:00) inversions
 378 generally exert stronger effects than evening (20:00) inversions, particularly in NWC (Figs. S128, S139). Occasional nighttime
 379 PM_{2.5} decreases under SBIs are observed at some NC/NEC stations, but these changes are not statistically significant.



380



381

382 Fig.8 Distribution of $PM_{2.5}$ concentration differences with and without temperature inversion. The larger circle indicates significance at the
 383 95% level (t -test)

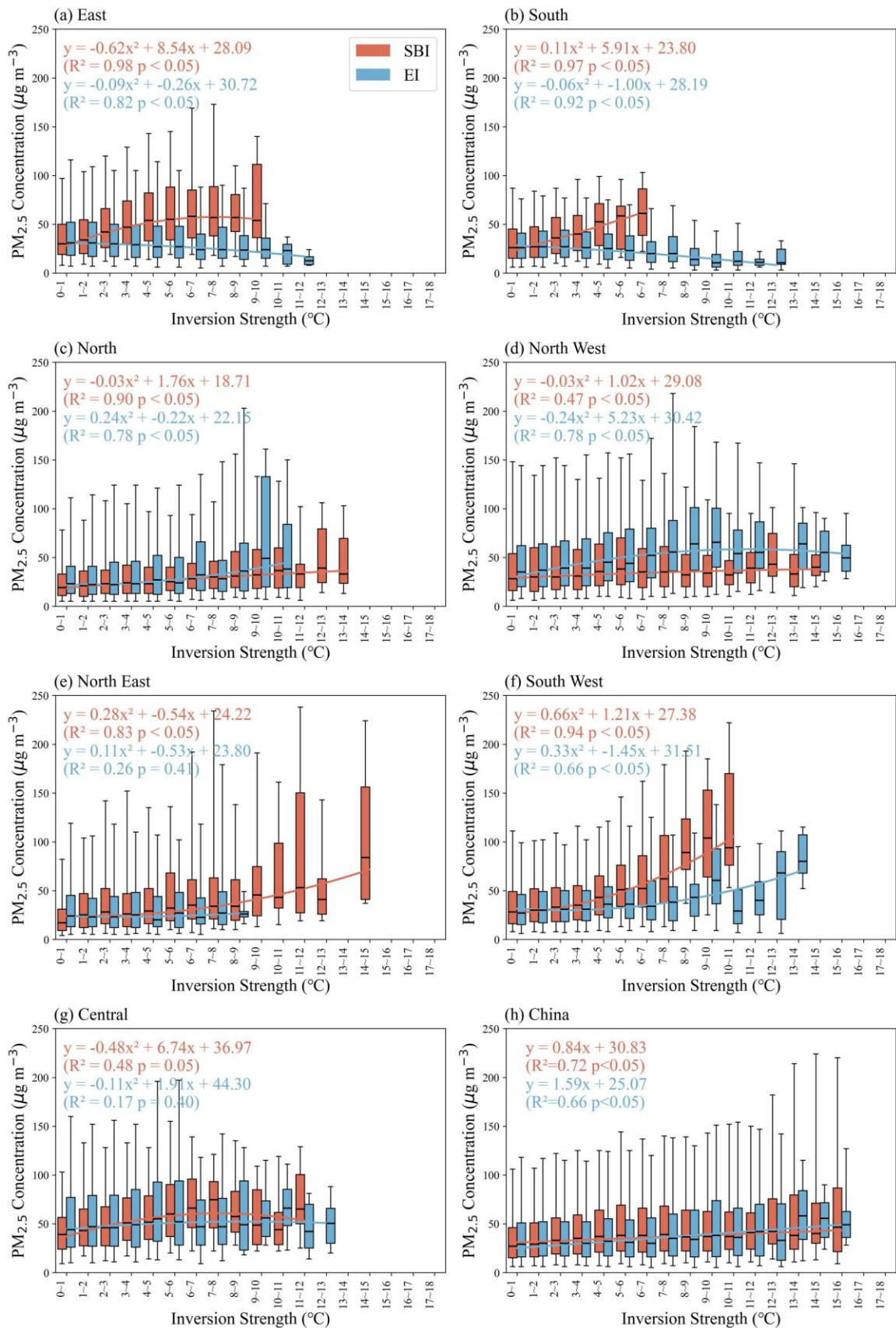
384

385 We quantified $PM_{2.5}$ responses to inversion parameters (strength, thickness) at 75 stations. Nationwide, $PM_{2.5}$ rises near-
 386 linearly with inversion strength for both SBIs and EIs (Fig. 9h): below 8 °C, SBIs exert the stronger effect; above 8 °C, EIs
 387 become more influential. Regionally, four response regimes emerge: Northern Inland China, Southeastern Coastal China,
 388 Central China, and Southwestern China. In EC/SC, SBI intensity correlates positively with $PM_{2.5}$ ($R^2 > 0.9$), whereas EI
 389 intensity correlates negatively ($R^2 > 0.8$); SBI strengths there seldom exceed 10 °C, far weaker than inland values. In NEC/NC,
 390 SBI strength can exceed 14 °C and is strongly coupled to $PM_{2.5}$. EI effects are mixed: NC shows a monotonic increase in $PM_{2.5}$
 391 with EI strength; NWC peaks at 10.9 °C (58.9 $\mu g m^{-3}$) then declines; NEC shows no significant correlation. In the SWC, both
 392 SBI and EI display a parabolic relationship with $PM_{2.5}$, with SBI exerting the larger enhancement (correlation up to 0.94). In
 393 Central China, overall fits are poor/non-significant, likely reflecting (i) the limited sample (four stations) and (ii) the region's
 394 role as a convergence zone receiving substantial inflow from surrounding regions—regional transport contributes >65% to
 395 $PM_{2.5}$ in cities such as Wuhan (Yu et al., 2020).

396

By contrast, inversion thickness shows a much weaker and less uniform association with $PM_{2.5}$ (Fig. S140). SBI thickness
 397 is generally positively correlated with $PM_{2.5}$ (except in NEC). For EI, significant thickness- $PM_{2.5}$ relationships appear only in
 398 NEC and NWC ($R^2 = 0.86$ and 0.92, respectively); elsewhere, EI thickness exerts negligible influence. Together, these results
 399 establish inversion strength—not thickness—as the dominant predictor of $PM_{2.5}$ accumulation (Fig. 9 vs. Fig. S140).₅

400 Thickness primarily defines the volume of the trapping layer: a deep but weak inversion can be eroded by mechanical
401 turbulence more readily than a shallow but intense one. This mechanism ensures that a stronger temperature gradient yields
402 greater static stability and more effective suppression of turbulent mixing, consistent with the mechanism that a stronger
403 temperature gradient yields greater static stability and more effective suppression of turbulent mixing (Liu et al., [2022](#)).
404 ~~Thickness primarily defines the volume of the trapping layer: a deep but weak inversion can be eroded by mechanical~~
405 ~~turbulence more readily than a shallow but intense one.~~



406

407 **Figure 9** Fitting relationship between inversion strength and PM_{2.5} concentration across seven regions of China from 2016 to 2021. The ends

408 of the boxes, the ends of the bars, and the short line across each box represent the 25th and 75th percentiles, the 5th and 95th percentiles,

409 and the median, respectively. Each strength interval contains a sample size ≥ 10 .

410 5 Conclusions

411 Temperature inversions (TIs) are widely recognized as a key meteorological regulator of near-surface $PM_{2.5}$, yet their
412 nationwide behaviour and impacts have remained incompletely characterized. Leveraging high-vertical-resolution radiosondes
413 from 75 stations (2016–2021) and collocated surface $PM_{2.5}$, we provide an observation-based assessment of inversion
414 frequency, intensity, thickness, and diurnal variability across China, and quantify how distinct inversion types modulate
415 pollution accumulation.

416 First, TIs are pervasive: the national annual means are 51.8% for frequency, 2.13 °C for strength, and 214 m for thickness.
417 Strong regional heterogeneity emerges. SBIs occur more frequently and are substantially stronger over inland northern regions
418 (annual mean 3.02 °C), whereas EIs prevail along the southeastern coast and are thicker (e.g., 235 m in Central China; 227 m
419 in South China). Low-level inversions are comparatively rare in the Southwest. Diurnally, inversions are more frequent,
420 stronger, and thicker at 08:00 BJT than at 20:00, with the SBI day–night contrast muted in summer and amplified in winter—
421 consistent with radiative control. Second, TIs materially elevate winter haze risk. Relative to non-inversion conditions, the
422 probability of a pollution event increases by 52% in winter, and the share of extreme events doubles, establishing TIs as a first-
423 order meteorological driver of both frequency and severity of winter haze in China. Third, the type of inversion matters. SBIs
424 robustly enhance $PM_{2.5}$ across most regions, reflecting efficient near-surface trapping under nocturnal stability. EIs show
425 regionally divergent behaviour: they enhance $PM_{2.5}$ in the north and northwest but are negatively associated with $PM_{2.5}$ in the
426 east and south, consistent with a transport-inhibition mechanism that limits northerly inflow under subsidence/warm-advection
427 regimes. Fourth, inversion strength is the dominant predictor of $PM_{2.5}$ accumulation, while thickness plays a secondary, region-
428 dependent role. Nationally, $PM_{2.5}$ increases near-linearly with strength-intensity for both SBI and EI; below 8 °C SBI effects
429 dominate, whereas above 8 °C EI effects strengthen. Thickness is generally weakly correlated with $PM_{2.5}$, except in select
430 regions (e.g., NEC/NWC for EI), underscoring that static stability (temperature gradient) governs ventilation more directly
431 than layer depth.

432 These findings offer concrete avenues for improving air pollution forecasting. (i) Improving the vertical resolution and
433 the predictive skill of temperature inversions in numerical models could enhance the forecast of air pollution events,
434 particularly in winter~~These findings offer concrete avenues for forecasting and control. (i) Incorporating real-time inversion~~
435 ~~diagnostics—especially intensity—into operational air quality models should improve short lead $PM_{2.5}$ forecasts and early-~~
436 ~~warning skill, particularly in winter.~~ (ii) Region-specific strategies are warranted: curbing evening–night emissions and
437 promoting nocturnal ventilation are likely most effective where SBIs dominate (northern basins/plains), whereas transport
438 management and synoptic-regime awareness may be more impactful in the southeast where EIs can isolate the boundary layer
439 from upwind inflow. (iii) The observed diurnal asymmetry suggests targeted mitigation during windows of maximum trapping
440 (pre-sunrise to morning transition).

441 Our assessment remains limited by sparser coverage over plateau terrain and the lack of vertical PM_{2.5} profiles, which
442 constrains diagnosis of aerosol layering and entrainment. Future work should augment radiosondes with Raman/HSRL lidar,
443 UAV or aircraft soundings, and assimilate inversion-aware stability metrics into kilometre-scale chemical transport models;
444 leverage geostationary multi-sensor diurnal sampling to resolve inversion evolution; and evaluate co-trends among inversions,
445 emissions, and climate-driven shifts in nocturnal cooling and synoptic patterns. These steps will sharpen causal attribution of
446 TI–pollution coupling and strengthen the forecast-to-policy pipeline for region-tailored air-quality management.

447
448 *Data availability.* The radiosonde data used in this study are available from the China Meteorological Administration (CMA).
449 The hourly ground-level PM_{2.5} concentration data can be obtained from the China National Environmental Monitoring Centre
450 (CNEMC; real-time platform: <https://www.cnemc.cn/en/>).

451
452 *Author contributions.* YF and HW designed the study. HH, JG, XZ and FM contributed to the observation data, provided
453 experimental assistance, and analyzed the methodology. YF wrote the paper with input from all the other authors.

454
455 *Competing interests.* The authors declare that they have no known competing financial interests or personal relationships that
456 could have appeared to influence the work reported in this paper.

457
458 *Acknowledgements.* This study was funded by the Sichuan Provincial Central Leading Local Science and Technology
459 Development Special Project (2025ZYD0179), the "Challenge and Command" China Meteorological Administration
460 (CMAJBGS202607), the Open Grants of China Meteorological Administration Radar Meteorology Key Laboratory
461 (2025ZD02), the Innovation Fund of the Jilin Field Research Station for Cloud Physics, China Meteorological
462 Administration/Jilin Provincial Key Laboratory of Weather Modification (M202504), and the Key Laboratory of Intelligent
463 Meteorological Observation Technology, China Meteorological Administration (ZNGC2025MS21).~~This study was funded by~~
464 ~~the Key Laboratory of Atmosphere Sounding, China Meteorological Administration (2023KLAS12M).~~

465
466 *Financial support.* This research has been supported by the Sichuan Provincial Central Leading Local Science and Technology
467 Development Special Project (2025ZYD0179), the "Challenge and Command" China Meteorological Administration
468 (CMAJBGS202607), the Open Grants of China Meteorological Administration Radar Meteorology Key Laboratory
469 (2025ZD02), the Innovation Fund of the Jilin Field Research Station for Cloud Physics, China Meteorological
470 Administration/Jilin Provincial Key Laboratory of Weather Modification (M202504), and the Key Laboratory of Intelligent
471 Meteorological Observation Technology, China Meteorological Administration (ZNGC2025MS21).~~This research has been~~
472 ~~supported by the Key Laboratory of Atmosphere Sounding, China Meteorological Administration (2023KLAS12M).~~

474 **References**

- 475 Aishajiang, A., Liang, F., Xu, H., Muhetaer, W., and Maimaitiaili, M.: Transport pathway of dust storm and its impact on air
476 quality in Hetian Oasis, *Acta Scientiae Circumstantiae*, 40, <https://doi.org/10.13671/j.hjkxxb.2020.0159>, 2020.
- 477 Chan, C. K. and Yao, X.: Air pollution in mega cities in China, *Atmospheric Environment*, 42, 1–42,
478 <https://doi.org/10.1016/j.atmosenv.2007.09.003>, 2008.
- 479 Chen, J., Lv, H., Wang, Q., Wang, G., Jia, K., Zhao, C., Shi, W., and Yan, X.: Revolutionizing Satellite Real-Time Air Pollution
480 Alerts through New On-Orbit System-on-Chip Technology, *Environ. Sci. Technol.*, 59, <https://doi.org/10.1021/acs.est.5c02470>,
481 2025.
- 482 Czarnecka, M., Nidzgorska-Lencewicz, J., and Rawicki, K.: Temporal structure of thermal inversions in Łeba (Poland), *Theor
483 Appl Climatol*, 136, 1–13, <https://doi.org/10.1007/s00704-018-2459-8>, 2019.
- 484 Deng, C., Qin, C., Li, Z., and Li, K.: Spatiotemporal variations of PM_{2.5} pollution and its dynamic relationships with
485 meteorological conditions in beijing-tianjin-hebei region, *Chemosphere*, 301, 134640,
486 <https://doi.org/10.1016/j.chemosphere.2022.134640>, 2022.
- 487 Feng, X., Wei, S., and Wang, S.: Temperature inversions in the atmospheric boundary layer and lower troposphere over the
488 Sichuan Basin, China: Climatology and impacts on air pollution, *Science of The Total Environment*, 726, 138579,
489 <https://doi.org/10.1016/j.scitotenv.2020.138579>, 2020.
- 490 Garcia, A., Santa-Helena, E., De Falco, A., De Paula Ribeiro, J., Gioda, A., and Gioda, C. R.: Toxicological Effects of Fine
491 Particulate Matter (PM_{2.5}): Health Risks and Associated Systemic Injuries—Systematic Review, *Water Air Soil Pollut*, 234,
492 <https://doi.org/10.1007/s11270-023-06278-9>, 2023.
- 493 Guo, J., Miao, Y., Zhang, Y., Liu, H., Li, Z., Zhang, W., He, J., Lou, M., Yan, Y., Bian, L., and Zhai, P.: The climatology of
494 planetary boundary layer height in China derived from radiosonde and reanalysis data, *Atmos. Chem. Phys.*, 16, 13309–13319,
495 <https://doi.org/10.5194/acp-16-13309-2016>, 2016.
- 496 Guo, J., Chen, X., Su, T., Liu, L., Zheng, Y., Chen, D., Li, J., Xu, H., Lv, Y., He, B., Li, Y., Hu, X.-M., Ding, A., and Zhai, P.:
497 The Climatology of Lower Tropospheric Temperature Inversions in China from Radiosonde Measurements: Roles of Black
498 Carbon, Local Meteorology, and Large-Scale Subsidence, *Journal of Climate*, 33, 9327–9350, [https://doi.org/10.1175/JCLI-
D-19-0278.1](https://doi.org/10.1175/JCLI-
499 D-19-0278.1), 2020.
- 500 Huang, Q., Chu, Y., and Li, Q.: Climatology of low-level temperature inversions over China based on high-resolution
501 radiosonde measurements, *Theor Appl Climatol*, 144, 415–429, <https://doi.org/10.1007/s00704-021-03536-w>, 2021.
- 502 Kahl, J. D.: Characteristics of the low-level temperature inversion along the Alaskan Arctic coast, *Intl Journal of Climatology*,
503 10, 537–548, <https://doi.org/10.1002/joc.3370100509>, 1990.
- 504 Kahl, J. D. W., Martinez, D. A., and Zaitseva, N. A.: Long-term variability in the low-level inversion layer over the arctic
505 ocean, *Int. J. Climatol.*, 16, 1297–1313, [https://doi.org/10.1002/\(SICI\)1097-0088\(199611\)16:11%253C1297::AID-
JOC86%253E3.0.CO;2-T](https://doi.org/10.1002/(SICI)1097-0088(199611)16:11%253C1297::AID-
506 JOC86%253E3.0.CO;2-T), 1996.
- 507 Kassomenos, P. A., Paschalidou, A. K., Lykoudis, S., and Koletsis, I.: Temperature inversion characteristics in relation to

- 508 synoptic circulation above Athens, Greece, *Environ Monit Assess*, 186, 3495–3502, [https://doi.org/10.1007/s10661-014-3632-](https://doi.org/10.1007/s10661-014-3632-x)
509 x, 2014.
- 510 Lagmiri, S. and Dahech, S.: Temperature Inversion and Particulate Matter Concentration in the Low Troposphere of Cergy-
511 Pontoise (Parisian Region), *Atmosphere*, 15, 349, <https://doi.org/10.3390/atmos15030349>, 2024.
- 512 Largeron, Y. and Staquet, C.: Persistent inversion dynamics and wintertime PM₁₀ air pollution in Alpine valleys, *Atmospheric*
513 *Environment*, 135, 92–108, <https://doi.org/10.1016/j.atmosenv.2016.03.045>, 2016.
- 514 Li, J., Chen, H., Li, Z., Wang, P., Fan, X., He, W., and Zhang, J.: Analysis of Low-level Temperature Inversions and Their
515 Effects on Aerosols in the Lower Atmosphere, *Adv. Atmos. Sci.*, 36, 1235–1250, <https://doi.org/10.1007/s00376-019-9018-9>,
516 2019.
- 517 Li, Y., Yan, J., and Sui, X.: Tropospheric temperature inversion over central China, *Atmospheric Research*, 116, 105–115,
518 <https://doi.org/10.1016/j.atmosres.2012.03.009>, 2012.
- 519 Liang, C., Zang, Z., Li, Z., and Yan, X.: An Improved Global Land Anthropogenic Aerosol Product Based on Satellite
520 Retrievals From 2008 to 2016, *IEEE Geosci. Remote Sensing Lett.*, 18, 944–948, <https://doi.org/10.1109/LGRS.2020.2991730>,
521 2021.
- 522 Liu, B., Ma, X., Ma, Y., Li, H., Jin, S., Fan, R., and Gong, W.: The relationship between atmospheric boundary layer and
523 temperature inversion layer and their aerosol capture capabilities, *Atmospheric Research*, 271, 106121,
524 <https://doi.org/10.1016/j.atmosres.2022.106121>, 2022.
- 525 Luo, N., Zhang, Y., Jiang, Y., Zuo, C., Chen, J., Zhao, W., Shi, W., and Yan, X.: Unveiling global land fine- and coarse-mode
526 aerosol dynamics from 2005 to 2020 using enhanced satellite-based monthly inversion data, *Environmental Pollution*,
527 <https://doi.org/10.1016/j.envpol.2024.123838>, 2024.
- 528 Ma, Y., Yao, W., and Huang, B.: Comparison of temperature and geopotential height records between 59 type and L-band
529 radiosonde systems, *Journal of Applied Meteorological Science*, 21, 214–220, [https://doi.org/10.3969/j.issn.1001-](https://doi.org/10.3969/j.issn.1001-7313.2010.02.011)
530 7313.2010.02.011, 2010.
- 531 Meng, X., Wei, Z., and Ye, C.: Variation Characteristics of Ambient Air Quality in China during 2013–2022, *Environmental*
532 *Monitoring and Forewarning*, 15, 1–7, <https://doi.org/10.3969/j.issn.1674-6732.02023.05.001>, 2023.
- 533 Miao, Y., Che, H., Zhang, X., and Liu, S.: Integrated impacts of synoptic forcing and aerosol radiative effect on boundary layer
534 and pollution in the Beijing–Tianjin–Hebei region, China, *Atmospheric Chemistry and Physics*, 20, 5899–5909,
535 <https://doi.org/10.5194/acp-20-5899-2020>, 2020.
- 536 Milionis, A. E. and Davies, T. D.: A five-year climatology of elevated inversions at Hemsby (UK), *Intl Journal of Climatology*,
537 12, 205–215, <https://doi.org/10.1002/joc.3370120209>, 1992.
- 538 Ministry of ecology and environment the people’s republic of China: Report on the State of the Ecology and Environment in
539 China 2022, Ministry of ecology and environment the people’s republic of China, 72 pp., 2022.
- 540 Morawska, L., Zhu, T., Liu, N., Amouei Torkmahalleh, M., De Fatima Andrade, M., Barratt, B., Broomandi, P., Buonanno, G.,
541 Carlos Belalcazar Ceron, L., Chen, J., Cheng, Y., Evans, G., Gavidia, M., Guo, H., Hanigan, I., Hu, M., Jeong, C. H., Kelly,
542 F., Gallardo, L., Kumar, P., Lyu, X., Mullins, B. J., Nordstrøm, C., Pereira, G., Querol, X., Yezid Rojas Roa, N., Russell, A.,
543 Thompson, H., Wang, H., Wang, L., Wang, T., Wierzbicka, A., Xue, T., and Ye, C.: The state of science on severe air pollution
544 episodes: Quantitative and qualitative analysis, *Environment International*, 156, 106732,

545 <https://doi.org/10.1016/j.envint.2021.106732>, 2021.

546 Palarz, A., Celiński-Mysław, D., and Ustrnul, Z.: Temporal and spatial variability of surface-based inversions over Europe
547 based on ERA -Interim reanalysis, *Intl Journal of Climatology*, 38, 158–168, <https://doi.org/10.1002/joc.5167>, 2018.

548 Peng, Y., Zhao, Y., Gao, N., Sheng, D., Tang, S., Zheng, S., and Wang, M.: Spatiotemporal evolution of PM_{2.5} and its
549 components and drivers in China, 2000–2023: effects of air pollution prevention and control actions in China, *Environmental*
550 *Geochemistry and Health*, 47, 69, <https://doi.org/10.1007/s10653-025-02375-2>, 2025.

551 Rendón, A. M., Salazar, J. F., Palacio, C. A., and Wirth, V.: Temperature Inversion Breakup with Impacts on Air Quality in
552 Urban Valleys Influenced by Topographic Shading, *Journal of Applied Meteorology and Climatology*, 54, 302–321,
553 <https://doi.org/10.1175/JAMC-D-14-0111.1>, 2015.

554 Rentschler, J. and Leonova, N.: Global air pollution exposure and poverty, *Nat Commun*, 14, 4432,
555 <https://doi.org/10.1038/s41467-023-39797-4>, 2023.

556 Schiemann, Luethi, and Schaer: Seasonality and Interannual Variability of the Westerly Jet in the Tibetan Plateau Region,
557 *Journal of climate*, 22, 2009.

558 Serreze, M., Kahl, J., and Schnell, R.: Low-Level Temperature Inversions of the Eurasian Arctic and Comparisons with Soviet
559 Drifting Station Data, *Journal of Climate*, 5, 615–629, [https://doi.org/10.1175/1520-0442\(1992\)005%3C0615:LLTIOT%3E2.0.CO;2](https://doi.org/10.1175/1520-0442(1992)005%3C0615:LLTIOT%3E2.0.CO;2), 1992.

561 Shao, M., Xu, X., Lu, Y., and Dai, Q.: Spatio-temporally differentiated impacts of temperature inversion on surface PM_{2.5} in
562 eastern China, *Science of The Total Environment*, 855, 158785, <https://doi.org/10.1016/j.scitotenv.2022.158785>, 2023.

563 Stull, R. B.: *An Introduction to Boundary Layer Meteorology*, , 0, 1988.

564 Sun, M., Xie, Z., Yao, X., Wang, S., and Dong, L.: Multilayer temperature inversion structures and their potential impact on
565 atmospheric pollution in northwest China, *Atmospheric Environment*, 343, 120998,
566 <https://doi.org/10.1016/j.atmosenv.2024.120998>, 2025.

567 Vihma, T., Kilpeläinen, T., Manninen, M., Sjöblom, A., Jakobson, E., Palo, T., Jaagus, J., and Maturilli, M.: Characteristics of
568 Temperature and Humidity Inversions and Low-Level Jets over Svalbard Fjords in Spring, *Advances in Meteorology*, 2011,
569 1–14, <https://doi.org/10.1155/2011/486807>, 2011.

570 Wallace, J. and Kanaroglou, P.: The effect of temperature inversions on ground-level nitrogen dioxide (NO₂) and fine
571 particulate matter (PM_{2.5}) using temperature profiles from the Atmospheric Infrared Sounder (AIRS), *Science of The Total*
572 *Environment*, 407, 5085–5095, <https://doi.org/10.1016/j.scitotenv.2009.05.050>, 2009.

573 WHO: WHO global air quality guidelines: particulate matter (PM_{2.5} and PM₁₀), ozone, nitrogen dioxide, sulfur dioxide and
574 carbon monoxide, 2021.

575 Wolf, T., Esau, I., and Reuder, J.: Analysis of the vertical temperature structure in the Bergen valley, Norway, and its connection
576 to pollution episodes, *J. Geophys. Res. Atmos.*, 119, <https://doi.org/10.1002/2014JD022085>, 2014.

577 Wu, W., Zha, Y., Zhang, J., Gao, J., and He, J.: A temperature inversion-induced air pollution process as analyzed from Mie
578 LiDAR data, *Science of The Total Environment*, 479–480, 102–108, <https://doi.org/10.1016/j.scitotenv.2014.01.112>, 2014.

579 Xu, T., Song, Y., Liu, M., Cai, X., Zhang, H., Guo, J., and Zhu, T.: Temperature inversions in severe polluted days derived
580 from radiosonde data in North China from 2011 to 2016, *Science of The Total Environment*, 647, 1011–1020,

581 <https://doi.org/10.1016/j.scitotenv.2018.08.088>, 2019.

582 Xu, T., Liu, B., Zhang, M., Song, Y., Kang, L., Wang, T., Liu, M., Cai, X., Zhang, H., and Zhu, T.: Temperature inversions in
583 China derived from sounding data from 1976 to 2015, *Tellus B: Chemical and Physical Meteorology*, 73, 1898906,
584 <https://doi.org/10.1080/16000889.2021.1898906>, 2021.

585 Yan, X., Liang, C., Jiang, Y., Luo, N., Zang, Z., and Li, Z.: A Deep Learning Approach to Improve the Retrieval of Temperature
586 and Humidity Profiles From a Ground-Based Microwave Radiometer, *IEEE Trans. Geosci. Remote Sensing*, 58, 8427–8437,
587 <https://doi.org/10.1109/TGRS.2020.2987896>, 2020.

588 Yan, X., Zang, Z., Jiang, Y., Shi, W., Guo, Y., Li, D., Zhao, C., and Husi, L.: A Spatial-Temporal Interpretable Deep Learning
589 Model for improving interpretability and predictive accuracy of satellite-based PM_{2.5}, *Environmental Pollution*, 273, 116459,
590 <https://doi.org/10.1016/j.envpol.2021.116459>, 2021.

591 Yan, X., Zuo, C., Li, Z., Chen, H. W., Jiang, Y., He, B., Liu, H., Chen, J., and Shi, W.: Cooperative simultaneous inversion of
592 satellite-based real-time PM_{2.5} and ozone levels using an improved deep learning model with attention mechanism,
593 *Environmental Pollution*, 327, 121509, <https://doi.org/10.1016/j.envpol.2023.121509>, 2023.

594 Yang, J. and Shao, M.: Impacts of Extreme Air Pollution Meteorology on Air Quality in China, *JGR Atmospheres*, 126,
595 e2020JD033210, <https://doi.org/10.1029/2020JD033210>, 2021.

596 Yang, Y., Li, Z., Guo, J., Wang, Y., Wu, H., Shang, Y., Wang, Y., Zhu, L., and Yan, X.: Revolutionizing Clear-Sky Humidity
597 Profile Retrieval with Multi-Angle-Aware Networks for Ground-Based Microwave Radiometers, *J Remote Sens*, 5, 0736,
598 <https://doi.org/10.34133/remotesensing.0736>, 2025.

599 Yin, P.-Y., Chang, R.-I., Day, R.-F., Lin, Y.-C., and Hu, C.-Y.: Improving PM_{2.5} Concentration Forecast with the Identification
600 of Temperature Inversion, *Applied Sciences*, 12, 71, <https://doi.org/10.3390/app12010071>, 2021.

601 Yu, C., Zhao, T., Bai, Y., Zhang, L., Kong, S., Yu, X., He, J., Cui, C., Yang, J., You, Y., Ma, G., Wu, M., and Chang, J.: Heavy
602 air pollution with a unique “non-stagnant” atmospheric boundary layer in the Yangtze River middle basin aggravated by
603 regional transport of PM_{2.5} over China, *Atmospheric Chemistry and Physics*, 20, 7217–7230, <https://doi.org/10.5194/acp-20-7217-2020>, 2020.

604

605 Zang, Z., Wang, W., You, W., Li, Y., Ye, F., and Wang, C.: Estimating ground-level PM_{2.5} concentrations in Beijing, China
606 using aerosol optical depth and parameters of the temperature inversion layer, *Science of The Total Environment*, 575, 1219–
607 1227, <https://doi.org/10.1016/j.scitotenv.2016.09.186>, 2017.

608 Zang, Z., Li, D., Guo, Y., Shi, W., and Yan, X.: Superior PM_{2.5} Estimation by Integrating Aerosol Fine Mode Data from the
609 Himawari-8 Satellite in Deep and Classical Machine Learning Models, *Science of The Total Environment*, 13, 2775,
610 <https://doi.org/10.3390/rs13142779>, 2021.

611 Zhang, J., Zheng, Y., Li, Z., Xia, X., and Chen, H.: A 17-year climatology of temperature inversions above clouds over the
612 ARM SGP site: The roles of cloud radiative effects, *Atmospheric Research*, 237, 104810,
613 <https://doi.org/10.1016/j.atmosres.2019.104810>, 2020.

614 Zhang, Y. H., Zhang, S. D., Yi, F., and Chen, Z. Y.: Statistics of lower tropospheric inversions over the continental United
615 States, *Ann. Geophys.*, 29, 401–410, <https://doi.org/10.5194/angeo-29-401-2011>, 2011.

616 Zhong, J., Zhang, X., Wang, Y., Sun, J., Zhang, Y., Wang, J., Tan, K., Shen, X., Che, H., Zhang, L., Zhang, Z., Qi, X., Zhao,
617 H., Ren, S., and Li, Y.: Relative contributions of boundary-layer meteorological factors to the explosive growth of PM_{2.5}

618 during the red-alert heavy pollution episodes in Beijing in December 2016, *J Meteorol Res*, 31, 809–819,
619 <https://doi.org/10.1007/s13351-017-7088-0>, 2017.

620 Zhong, J., Zhang, X., Dong, Y., Wang, Y., Liu, C., Wang, J., Zhang, Y., and Che, H.: Feedback effects of boundary-layer
621 meteorological factors on cumulative explosive growth of PM_{2.5} during winter heavy pollution episodes in Beijing from 2013
622 to 2016, *Atmos. Chem. Phys.*, 18, 247–258, <https://doi.org/10.5194/acp-18-247-2018>, 2018.

623 Zou, J., Chen, H. W., Li, H., Wang, Q., Wang, G., Jia, K., Chen, Z., Zhao, C., Shi, W., Yang, Y., Tang, Y., Chen, J., Zhang, Y.,
624 Xu, T., Wang, Y., Liu, G., and Yan, X.: Amplified urban heat island effect in southern china's old towns following atmospheric
625 regulation policies, *Sustainable Cities and Society*, 131, 106675, <https://doi.org/10.1016/j.scs.2025.106675>, 2025.

626 Zuo, C., Chen, J., Zhang, Y., Jiang, Y., Liu, M., Liu, H., Zhao, W., and Yan, X.: Evaluation of four meteorological reanalysis
627 datasets for satellite-based PM_{2.5} retrieval over China, *Atmospheric Environment*, 305, 119795,
628 <https://doi.org/10.1016/j.atmosenv.2023.119795>, 2023.

629